Supplement of Atmos. Meas. Tech., 15, 2857–2874, 2022
https://doi.org/10.5194/amt-15-2857-2022-supplement

Atmospheric Measurement Techniques
Open Access
EGU

Supplement of

Fragment ion–functional group relationships in organic aerosols using aerosol mass spectrometry and mid-infrared spectroscopy

Amir Yazdani et al.

Correspondence to: Satoshi Takahama (satoshi.takahama@epfl.ch) and Imad El Haddad (imad.el-haddad@psi.ch)

S1 Methodology diagrams

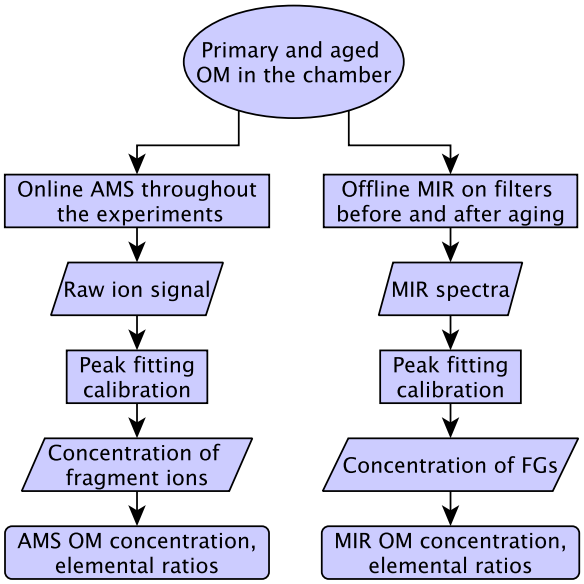

Figure S1. Diagram showing the MIR and AMS measurements of bulk OM and the initial postprocessing. Parallelograms, rectangles, and rounded rectangles show data, processes, and final postprocessed data, respectively.

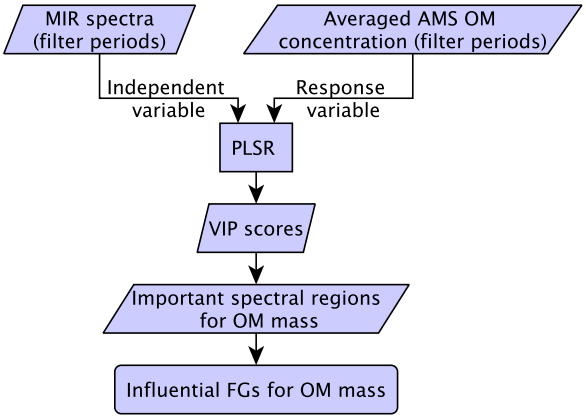

Figure S2. Diagram showing how the MIR spectra and AMS OM estimates are combined to determine the influential FGs.

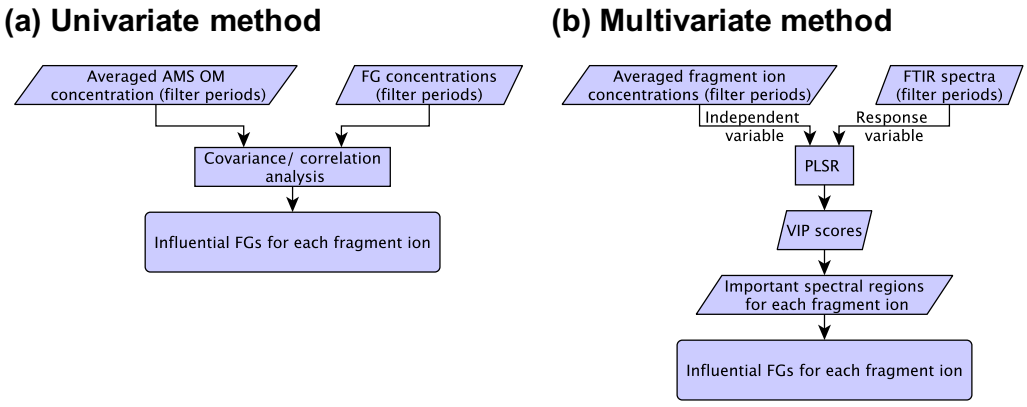

Figure S3. Diagrams showing how (a) MIR FG abundances or (b) MIR spectra are combined with the concentration of AMS fragment ions to determine which FGs produce certain fragment.

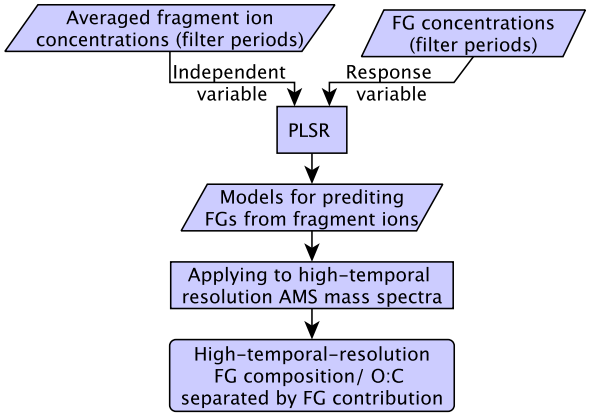

Figure S4. Diagram showing how high-temporal-resolution FG compositions are calculated by combining AMS and MIR measurements.

S2 AMS fragment ion-FG connections

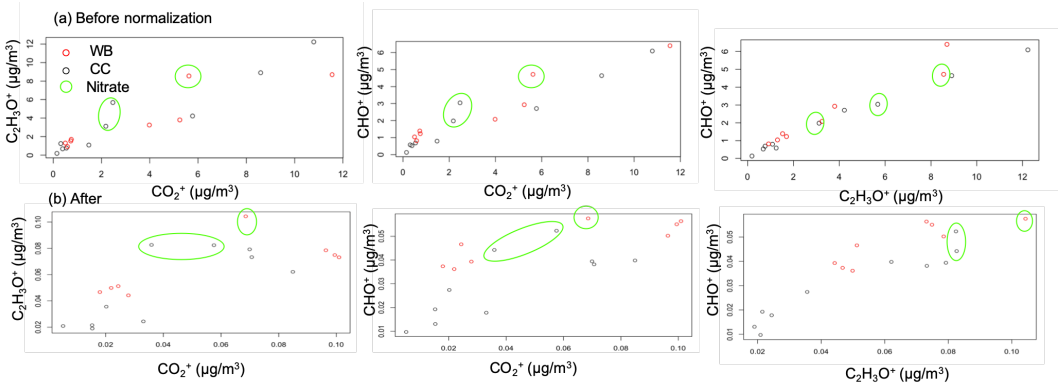

Figure S5. Scatter plot highlighting the correlation between major AMS mass fragments before and after normalization by total AMS OM. Green circles show the experiments for which the nitrate radical was used as oxidant.

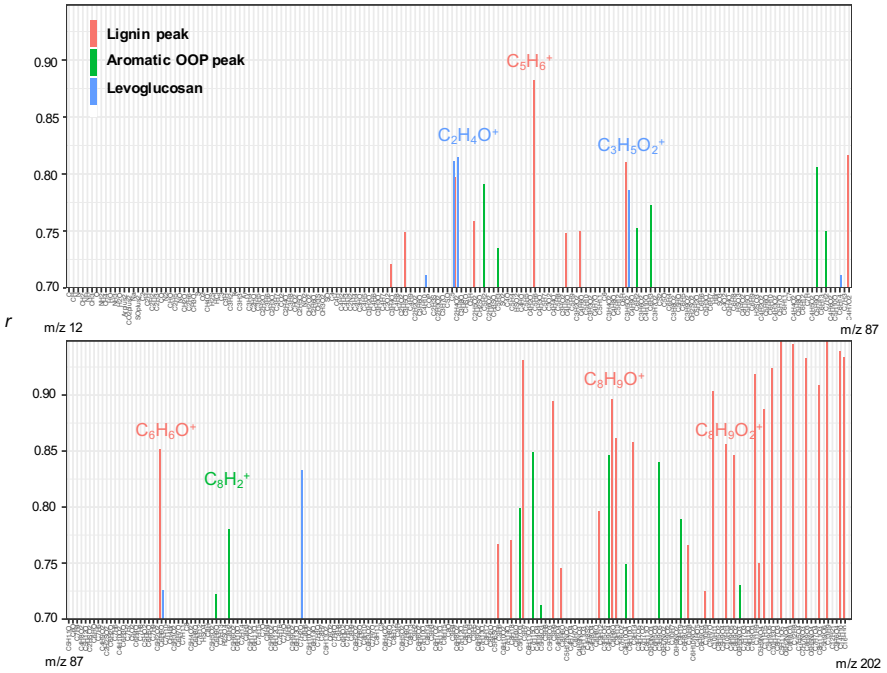

Figure S6. Barplot showing the Pearson correlation coefficients of lignin, levoglucosan and out-of-plane aromatic peaks in the MIR spectra and the concentration of AMS fragment ions. Only fragments with $r > 0.7$ have been shown.

Fig S8 shows the results of multivariate linear regressions that regress standardized (unit standard deviation and zero mean) FG abundances against standardized concentrations of three major fragments (and vice versa). The parameter selection is done using an stepwise algorithm working based on the Akaike information criterion (AIC). Only experiments with the hydroxyl

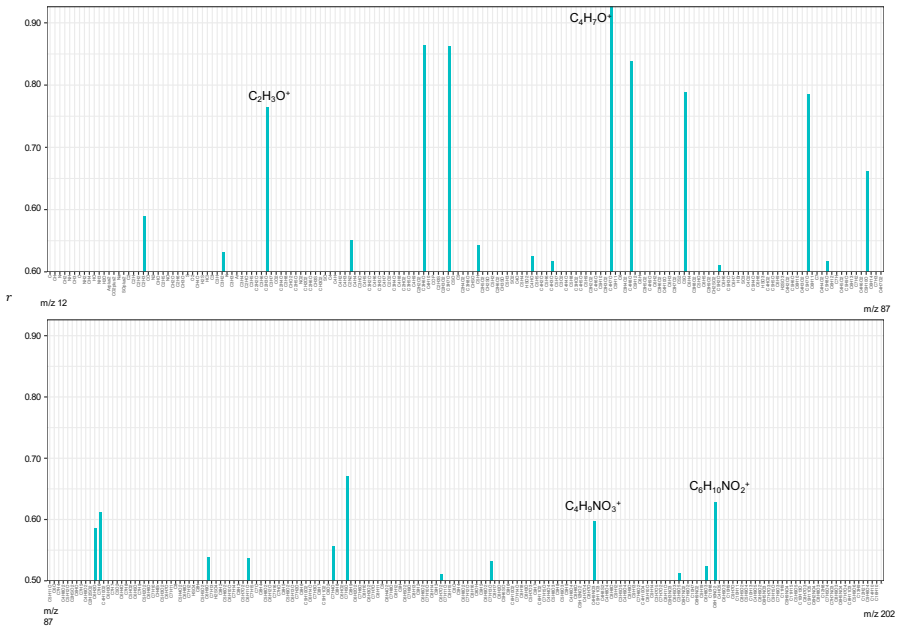

Figure S7. Barplot showing the Pearson correlation coefficient of $RONO_2$ peak in MIR spectra and the concentration of AMS organic fragment ions. Only fragments with $r > 0.5$ have been shown.

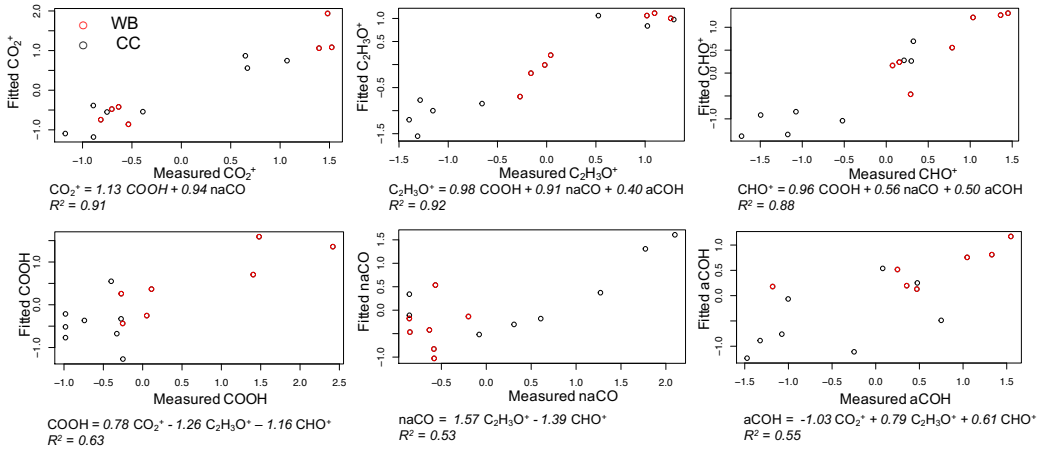

Figure S8. Scatter plots showing the measured and calculated AMS fragment concentrations using MIR FG concentrations and vice versa. The FG and fragment concentrations are standardized (zero mean and unit standard deviation) to make regression coefficients comparable. Regression equations are shown below each plot. The experiments for which the nitrate radical was been used have been omitted due to causing poor fit results.

radical are considered as aging with the nitrate radical causes the mentioned fragments to vary significantly without affecting the abundance of oxygenated FGs except organonitrates.

S3 PLSR models

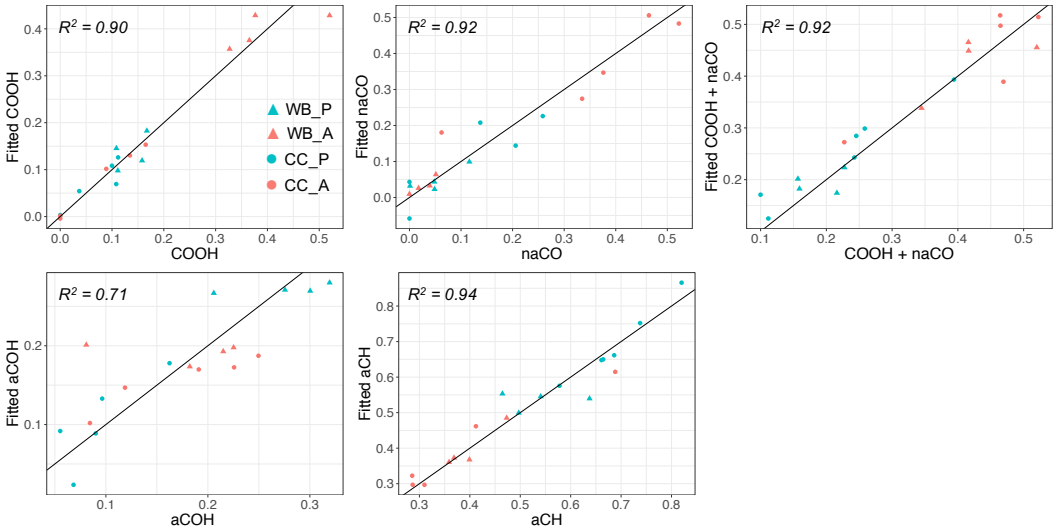

Figure S9. Scatter plots showing fitted (PLSR models) normalized functional group composition using AMS mass spectra against their values from the MIR peak fitting.

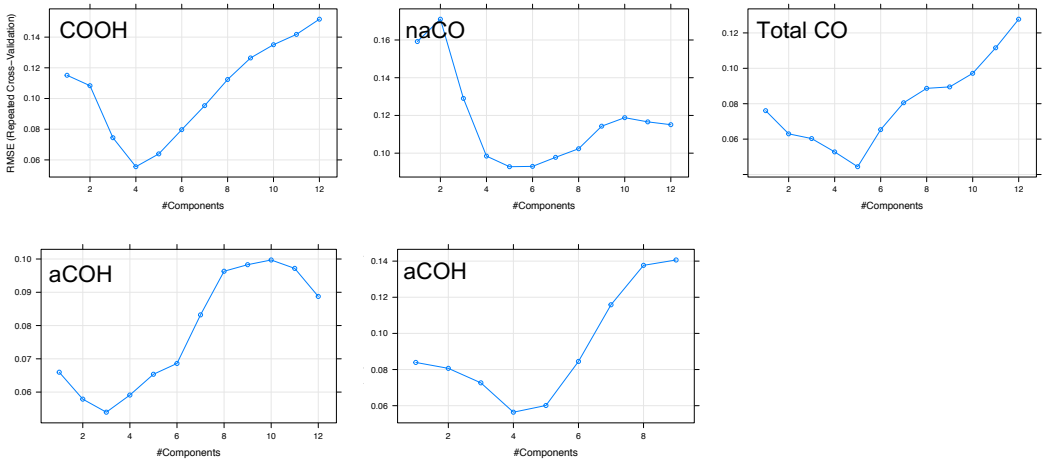

Figure S10. Plots showing the root mean squared error (RMSE) of predictions in the 10-fold cross validation for different number of latent variables in the PLSR models. The resulting PLSR models are used to predict normalized FG abundances using the AMS spectra.

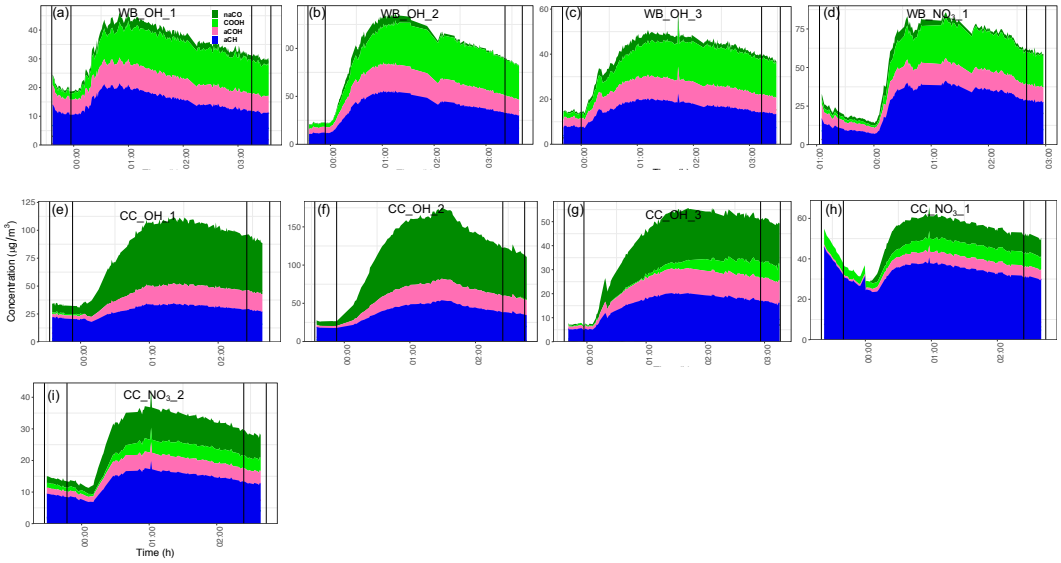

Figure S11. Time series of high-resolution stacked absolute functional group concentrations calculated using the AMS mass spectra. Total CO refers to the sum of COOH and naCO. The naming is the same as Fig. 4. The absolute concentrations are calculated by multiplying normalized concentrations by the total AMS OM and are not corrected for chamber wall losses.

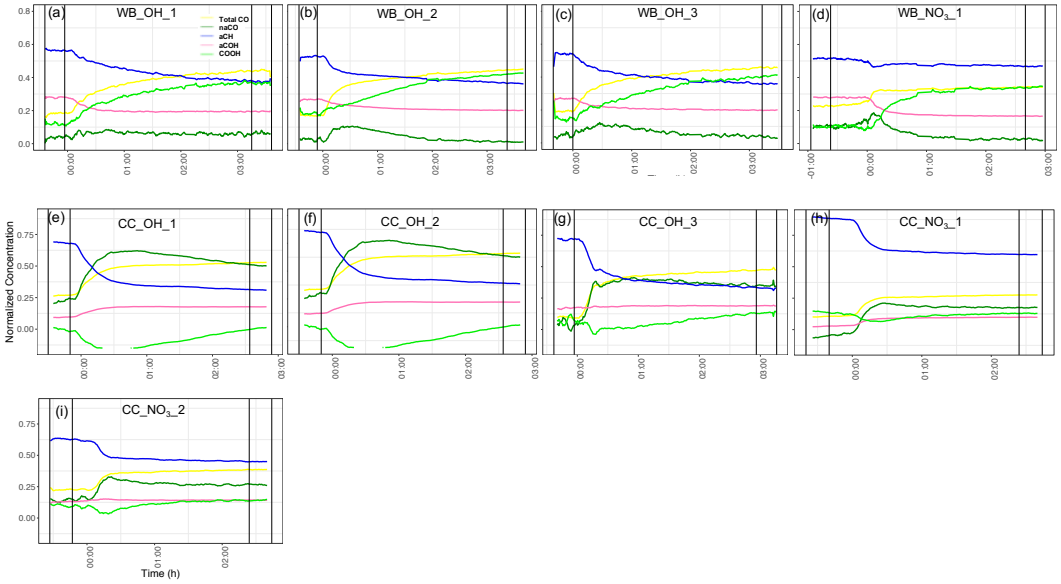

Figure S12. Time series of high-resolution normalized functional group concentrations calculated using the AMS mass spectra. Total CO refers to the sum of COOH and naCO. Vertical black lines show the filter sampling periods before and after aging. The naming is the same as Fig. 4 of the main manuscript. The time zero indicates the start of chemical aging.

As can be seen from Fig. S12, the predicted COOH concentrations are slightly negative for two CC experiments (CC_OH_1 and CC_OH_2) during the course of aging. These unphysical values, which are not substantial compared to total OM con-

centration (up to 15 % of total OM), might be attributed to: uncertainties of each instrument especially uncertainties in MIR COOH estimation for primary CC samples, model uncertainties (especially as models were developed using very different experiments), and errors introduced due to the use of models to predict compositions fairly different from those of filter sampling periods. However, the dynamic trend of COOH is still captured in these cases.

Figure S13 compares the oxidation trajectories from AMS and the reconstructed trajectories from the elemental ratios calculated from the interpolated functional groups. The constructed trajectories are able to capture the curvatures observed in the original trajectories although some discrepancies are observed in the absolute values.

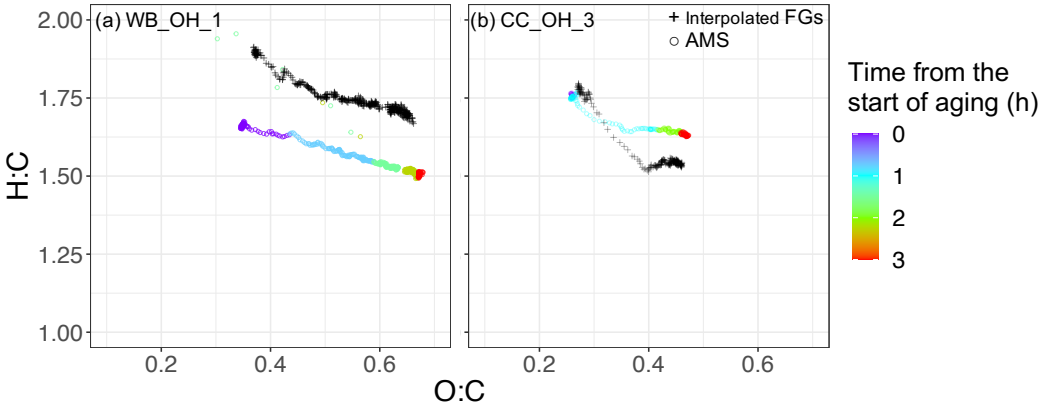

Figure S13. Comparison between van Krevelen trajectories from the AMS elemental ratios (circle) and elemental ratios reconstructed from the interpolated functional groups (cross) for a WB and a CC experiment.